Journal of Electrotechnology, Electrical Engineering and Management (2024)
Clausius Scientific Press, Canada
DOI: 10.23977/jeeem.2024.070106
ISSN 2560-6697 Vol. 7 Num. 1

# *Performance Study of Coaxial Dual-Nozzle Ejector Based on Automatic Simulation Platform*

**Liu Yuxiang[1,a,*], Zhang Tong[1,2,b]**

[1]*School of Automotive Studies, Tongji University, Shanghai, China*
[2]*Yangtze Delta Region Institute of Tsinghua University, Jiaxing, Zhejiang, 314006, China*
[a]*2131579@tongji.edu.cn*, [b]*tzhang@tongji.edu.cn*
[*]*Corresponding author*

***Keywords:*** Fuel cell, coaxial dual-nozzle ejector, automatic simulation

***Abstract:*** Proton exchange membrane fuel cell (PEMFC) vehicles are considered the ultimate form of automotive development due to their zero emissions and high energy conversion efficiency. The hydrogen supply system is crucial to the operation of PEMFC vehicles; efficient hydrogen supply improves hydrogen utilization, increases the hydrogen equivalence ratio, and reduces water blockage on the anode side. Ejectors, with their simple structure, small size, and no parasitic power, have attracted widespread attention. This paper establishes an automatic simulation platform for coaxial nozzle ejectors to study the impact of different operating conditions on ejector performance, and compares the working performance of coaxial nozzle ejectors with traditional single-nozzle ejectors under different loads.

## 1. Introduction

The extensive use of fossil fuels is a significant cause of excessive carbon emissions. Therefore, it is imperative for automobiles, as important means of transportation and production tools, to break away from their reliance on fossil fuels such as gasoline and diesel, and to find a new, clean, and emission-free power source[1-2]. Proton exchange membrane fuel cell (PEMFC) systems, with their high power density, efficiency, and zero pollution emissions, are considered a green power generation system[3-4]. The hydrogen supply system is a crucial component of the PEMFC system, and research on the hydrogen supply system helps to enhance the performance of the fuel cell system, with the ejector being a focus of research. Introducing an ejector into the hydrogen recirculation system helps to improve fuel utilization efficiency [5].

In the field of ejector research, significant efforts have been made by predecessors. Some studies have delved deeply into the principles of ejectors, providing guidance for the subsequent design of ejectors[6-7]; others have explored the relationship between ejector dimensions and performance, investigating the impact of geometric parameters on the internal flow patterns within ejectors[8-10]. With the advancement of technology, fuel cell systems now impose higher demands on ejectors. Current research is dedicated to expanding the working range of ejectors. For instance, Bruuner[11] proposed a geometrically variable ejector, Kim[12] designed a hydrogen recirculation system with multiple ejectors for small fuel cell vehicles, and Han[13] introduced multi-nozzle ejectors…This

paper will focus on the coaxial dual-nozzle ejector, designing an automatic simulation platform to study the impact of operating conditions on ejector performance.

The SIMULIA ISIGHT was first developed in the 1980's by Dr. Siu S. Tong of MIT. ISIGHT does not compute, but is more like a "software robot" that builds building blocks to link the software that needs to be operated according to the developer's own wishes. In this way, all the software required for an engineering application is assembled into an automated simulation process. Compared with other similar software, it provides a visual construction interface, so that users can more quickly grasp the operation and application of the software. At the same time, ISIGHT also provides an interface with most of the mainstream modeling and simulation software, making it more compatible. With this software, developers can quickly build complex simulation and analysis processes visually by dragging and dropping, and set and modify design variables and design goals by editing the data tables in each software, and automatically carry out multiple loop iterations according to the given parameters.

In addition, ISIGHT provides optimization algorithm packages such as Design of Experiments (DOE), Optimization Design, and Approximation Models to help users understand the design space of the product and clarify the relationship between design variables and design goals, so as to realize multi-disciplinary multi-objective optimization. In this paper, SIMULIA ISIGHT is used to build a fully automated simulation platform for the effect of operating conditions on the performance of a coaxial nozzle ejector, which fully improves the simulation efficiency and aids in the analysis based on the correlation mapping.

The automatic simulation platform in this paper is based on ISIGHT, which links the modeling software CATIA, meshing software ICEM and fluid simulation software FLUENT required in the simulation process, and modifies the parameters of design variables through the script macro files of the three. This automatic simulation platform can save developers' time consumed by repetitive operations and improve the efficiency of product development. In the process of building the platform, it is necessary to prepare the driver files of ISIGHT for each software and the script macro files of the software itself, and input the above files into ISIGHT, and the specific building logic is shown in the figure 1.

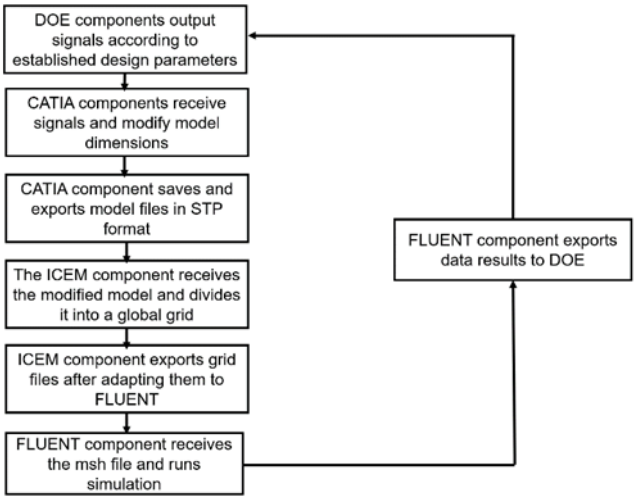


Figure 1: Automated simulation platform building logic

The driver file of the software runs in bat format, and the compilation code is concise and efficient. CATIA modifies the parameters in the macro file by calling the built-in secondary development and compilation language VBS, so as to change the structural parameters of the model in a quick way. ICEM realizes automatic and quick mesh division by modifying the rpl macro file, which can record the parameter settings of the global mesh division, but it can only generate non-structural meshes,

mostly tetrahedral meshes, and cannot realize full hexahedral meshing for irregular models. However, it can only generate non-structural meshes, and the mesh shapes are mostly tetrahedral, so it is impossible to realize full hexahedral meshing for irregular models. Therefore, in this paper, only part of the functions of the platform are used, and based on the optimized structural parameter model of the best ejector, the simulation boundary conditions are modified in the FLUENT component, and the changes in the performance of the ejector are observed under different operating conditions and loading currents. The completed automated simulation platform is shown in Figure 2.

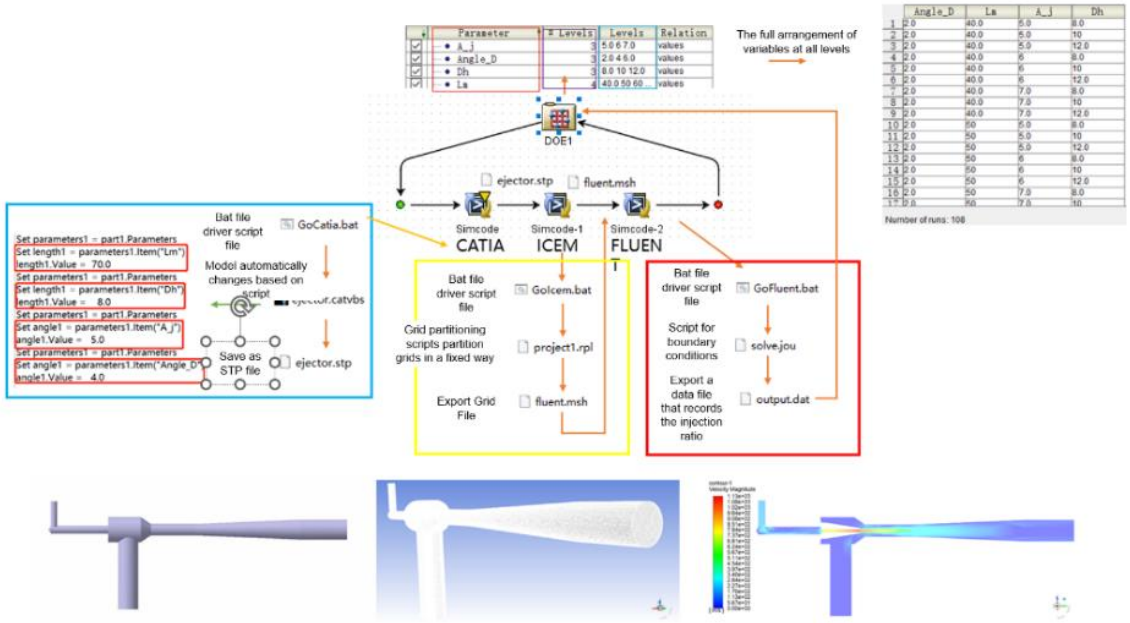


Figure 2: Automated simulation platform

## 2. Simulation results

### 2.1 Effect of primary inflow port temperature on elicitor performance

The primary flow hydrogen of the ejector is supplied by a high-pressure hydrogen cylinder. When the high-pressure hydrogen arrives at the front end of the proportional valve after two pressure adjustments, the gas pressure is reduced from 350 bar to a set value of 11 bar, and the temperature of the hydrogen gas decreases significantly during the process. In order to investigate the effect of primary flow temperature on the performance of the coaxial nozzle ejector under different loads, the temperature variation range was selected to be from 295K to 355K, with the values taken at 15K intervals, and the four conditions of 60A and 120A under low loads as well as 360A and 600A under medium and high loads were determined as the values of the variable loads.

Figure 3 shows the user parameter customization interface in ISIGHT, which can be invoked by modifying the Design of Experiments method in the DOE component. The method is customized by extracting and determining the parameters of the variables required by the user in the Simcode component, and ISIGHT will automatically update the variables according to the number table, and the calculation results of the target output will be automatically recorded. As shown in Fig. 3, which contains the parameters defined for the change of working conditions: inlet flow rate $mf_1$ and the dual nozzles $mf_2$, ejector outlet pressure and secondary inflow pressure, and nozzle inlet temperatures $t_1$ and $t_2$, the calculation process and results are shown in the figure 4.

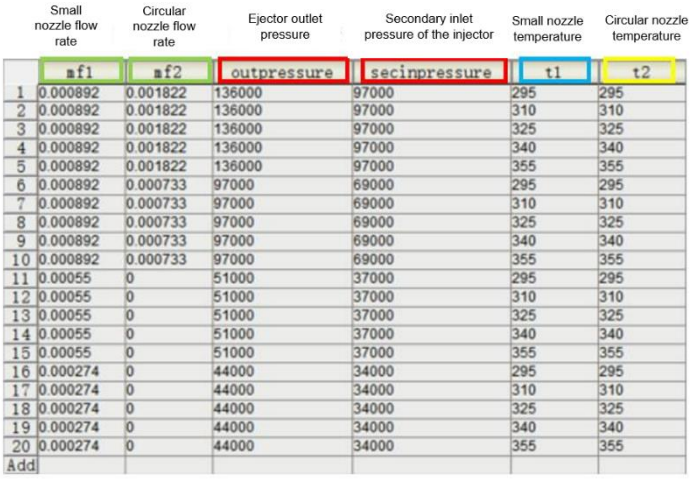


| | mf1 | mf2 | outpressure | secinpressure | t1 | t2 |
|---|---|---|---|---|---|---|
| 1 | 0.000892 | 0.001822 | 136000 | 97000 | 295 | 295 |
| 2 | 0.000892 | 0.001822 | 136000 | 97000 | 310 | 310 |
| 3 | 0.000892 | 0.001822 | 136000 | 97000 | 325 | 325 |
| 4 | 0.000892 | 0.001822 | 136000 | 97000 | 340 | 340 |
| 5 | 0.000892 | 0.001822 | 136000 | 97000 | 355 | 355 |
| 6 | 0.000892 | 0.000733 | 97000 | 69000 | 295 | 295 |
| 7 | 0.000892 | 0.000733 | 97000 | 69000 | 310 | 310 |
| 8 | 0.000892 | 0.000733 | 97000 | 69000 | 325 | 325 |
| 9 | 0.000892 | 0.000733 | 97000 | 69000 | 340 | 340 |
| 10 | 0.000892 | 0.000733 | 97000 | 69000 | 355 | 355 |
| 11 | 0.00055 | 0 | 51000 | 37000 | 295 | 295 |
| 12 | 0.00055 | 0 | 51000 | 37000 | 310 | 310 |
| 13 | 0.00055 | 0 | 51000 | 37000 | 325 | 325 |
| 14 | 0.00055 | 0 | 51000 | 37000 | 340 | 340 |
| 15 | 0.00055 | 0 | 51000 | 37000 | 355 | 355 |
| 16 | 0.000274 | 0 | 44000 | 34000 | 295 | 295 |
| 17 | 0.000274 | 0 | 44000 | 34000 | 310 | 310 |
| 18 | 0.000274 | 0 | 44000 | 34000 | 325 | 325 |
| 19 | 0.000274 | 0 | 44000 | 34000 | 340 | 340 |
| 20 | 0.000274 | 0 | 44000 | 34000 | 355 | 355 |
| Add | | | | | | |

Figure 3: User-defined parameters

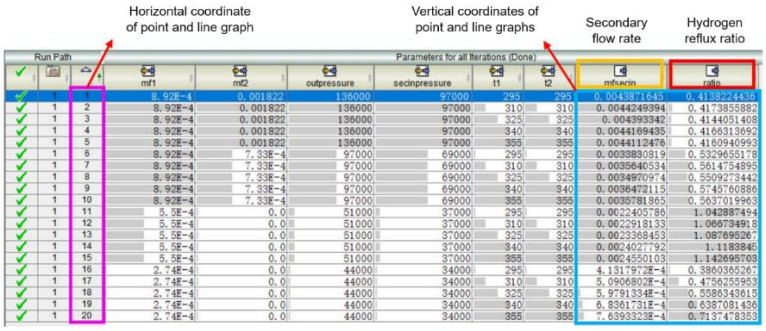


| | | | mf1 | mf2 | outpressure | secinpressure | t1 | t2 | mfsecin | rate |
|---|---|---|---|---|---|---|---|---|---|---|
| ✓ | 1 | 1 | 8.92E-4 | 0.001822 | 136000 | 97000 | 295 | 295 | 0.0043871645 | 0.4138224438 |
| ✓ | 1 | 2 | 8.92E-4 | 0.001822 | 136000 | 97000 | 310 | 310 | 0.0044249394 | 0.417385588 |
| ✓ | 1 | 3 | 8.92E-4 | 0.001822 | 136000 | 97000 | 325 | 325 | 0.004393342 | 0.4144051408 |
| ✓ | 1 | 4 | 8.92E-4 | 0.001822 | 136000 | 97000 | 340 | 340 | 0.0044169435 | 0.4166313692 |
| ✓ | 1 | 5 | 8.92E-4 | 0.001822 | 136000 | 97000 | 355 | 355 | 0.0044112476 | 0.4160940993 |
| ✓ | 1 | 6 | 8.92E-4 | 7.33E-4 | 97000 | 69000 | 295 | 295 | 0.0033883819 | 0.5329655178 |
| ✓ | 1 | 7 | 8.92E-4 | 7.33E-4 | 97000 | 69000 | 310 | 310 | 0.0035640534 | 0.5614754895 |
| ✓ | 1 | 8 | 8.92E-4 | 7.33E-4 | 97000 | 69000 | 325 | 325 | 0.003497074 | 0.550927344 |
| ✓ | 1 | 9 | 8.92E-4 | 7.33E-4 | 97000 | 69000 | 340 | 340 | 0.0036472115 | 0.5745760886 |
| ✓ | 1 | 10 | 8.92E-4 | 7.33E-4 | 97000 | 69000 | 355 | 355 | 0.0035781865 | 0.5637019963 |
| ✓ | 1 | 11 | 5.5E-4 | 0.0 | 51000 | 37000 | 295 | 295 | 0.0022405786 | 1.042887494 |
| ✓ | 1 | 12 | 5.5E-4 | 0.0 | 51000 | 37000 | 310 | 310 | 0.0022918133 | 1.066734918 |
| ✓ | 1 | 13 | 5.5E-4 | 0.0 | 51000 | 37000 | 325 | 325 | 0.0023368453 | 1.087698267 |
| ✓ | 1 | 14 | 5.5E-4 | 0.0 | 51000 | 37000 | 340 | 340 | 0.0024027792 | 1.1183846 |
| ✓ | 1 | 15 | 5.5E-4 | 0.0 | 51000 | 37000 | 355 | 355 | 0.0024550103 | 1.142695703 |
| ✓ | 1 | 16 | 2.74E-4 | 0.0 | 44000 | 34000 | 295 | 295 | 4.1317972E-4 | 0.3860365267 |
| ✓ | 1 | 17 | 2.74E-4 | 0.0 | 44000 | 34000 | 310 | 310 | 5.0906802E-4 | 0.4756255953 |
| ✓ | 1 | 18 | 2.74E-4 | 0.0 | 44000 | 34000 | 325 | 325 | 5.9791334E-4 | 0.5586343615 |
| ✓ | 1 | 19 | 2.74E-4 | 0.0 | 44000 | 34000 | 340 | 340 | 6.8361731E-4 | 0.6387081436 |
| ✓ | 1 | 20 | 2.74E-4 | 0.0 | 44000 | 34000 | 355 | 355 | 7.6393323E-4 | 0.7137473353 |

Figure 4: Table summarizing the results of primary stream temperature change calculations

Figure 4 is the summary table corresponding to the calculation results of Figure 3, which records the secondary flow rate $mf_{secin}$ of the ejector and the hydrogen recirculation ratio corresponding to the changing primary flow inlet temperature under different loads. ISIGHT will automatically plot the point-line diagram shown in Figure 5 based on this table. In the diagram, the horizontal axis corresponds to the sequence number associated with the Run Path in the summary table, representing the trend of changes in the primary flow inlet temperature of the fuel stack under different loads, while the vertical axis corresponds to the secondary flow rate and hydrogen recirculation ratio. Observing this diagram, it can be found that as the load current decreases, the impact of the primary flow temperature change on the ejector's secondary flow rate and the hydrogen recirculation ratio gradually increases. When the load current is 600A, the change in primary flow temperature has a smaller impact on the secondary flow rate and the hydrogen recirculation ratio, with the maximum secondary flow rate being 4.425 g and the minimum flow rate being 4.387 g, an increase of only 0.86%. When the load current decreases to 360A, there is a noticeable fluctuation in the secondary flow rate and hydrogen recirculation ratio, showing a trend of increasing with the rising temperature, where the growth rate of the secondary flow rate is 7.8%. As the load current further decreases, the primary flow temperature of the ejector and the hydrogen recirculation ratio are in complete positive correlation, with the growth rate of hydrogen recirculation ratio being 9.59% at 120A and 84.97% at 60A, corresponding to the orange and red circles in the diagram.

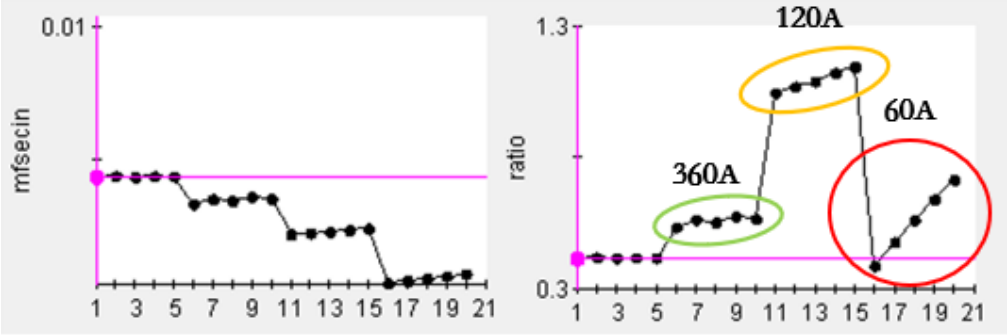


Figure 5: Trends of ejector performance parameter ratios with primary flow temperatures

The possible reason for the observed phenomenon is that when the temperature of the primary flow fluid increases and the nozzle supply pressure remains unchanged, the velocity of the primary flow increases. According to Bernoulli's equation (Formula 1) and the gas state equation, when the fluid temperature rises, the fluid density decreases. To maintain the total pressure rise unchanged, the fluid velocity will increase at this time. Therefore, the working performance of the ejector in the low load section correspondingly improves. However, at high load sections, the primary flow pressure is greater, and the fluid kinetic energy does not change significantly with temperature, limiting the range of velocity changes. Therefore, the ejecting capacity of the ejector will not show significant changes.

$$p + \rho g h + \frac{1}{2}\rho v^2 = c \tag{1}$$

ISIGHT will generate a Pareto chart and a variable relationship impact graph based on the above calculation results, as shown in Figures 6 and 7. Researchers can determine the contribution degree and the positive or negative effects of each variable on the dependent variable through both. The Pareto chart can fit a polynomial between independent and dependent variables using the multivariate linear regression method, where the vertical axis represents the terms in the polynomial, and the horizontal axis represents the contribution of these terms to the dependent variable, with blue indicating positive and red indicating negative. From this chart, it is found that the outlet pressure and the primary flow inlet flow rate contribute the most to the secondary flow rate and hydrogen recirculation ratio, followed by the primary flow inlet temperature. The ejector outlet pressure has a positive effect on the secondary flow rate but a negative effect on the hydrogen recirculation ratio, with the primary flow volume having the opposite effect, which is consistent with the actual situation.

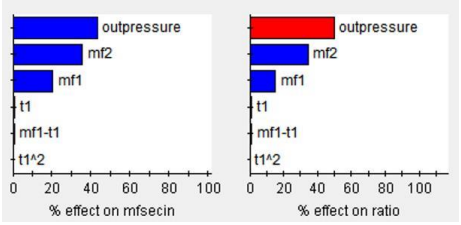


Figure 6: Pareto Figure

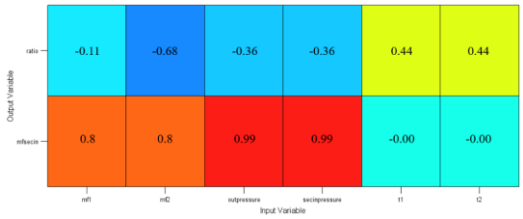


Figure 7: Plot of primary flow temperature change variables

In the variable relationship graph, the horizontal axis represents the specified independent variable, while the vertical axis represents the response dependent variable. The positivity or negativity of the values represents the effect's direction, and the magnitude represents the degree of impact of the independent variable on the dependent variable. Observing Figure 7, compared to the primary flow inlet temperature, changes in the fuel stack load current have a greater impact on the secondary flow rate, which is consistent with the data in Figures 4 and 5. Isolating changes in the primary flow inlet temperature has a minor numerical impact on the secondary flow rate, but when the fuel stack undergoes operational mode switching, there is a stepwise increase in the secondary flow rate. The primary flow inlet temperature has a significant effect on the ejector's hydrogen recirculation ratio, showing a positive correlation. However, with the increase in load current, except for the increase in hydrogen recirculation ratio between 60 A and 120 A due to operational mode switching, this value tends to decrease.

To summarize, the ejector can not pay attention to the primary inflow temperature when the stack is under high load, but it needs to be increased appropriately in the low load section. Especially in low-temperature environment, it is necessary to set up a heating device in front of the pilot proportional valve to avoid water vapor condensation and icing blocking the anode flow channel of the battery due to the low temperature of the inlet, which leads to the decrease of the temperature of the secondary flow.

## 2.2 Influence of secondary inflow port temperature on elicitor performance

We need to explore the effect of secondary flow temperature on the performance of the ejector. In this paper, according to the experimental data, the selected temperature change range is 320K to 360K, every increase of 10 K to take the value of a time, the selection of the working conditions of the power pile with the above to maintain consistency, the primary flow temperature is determined to be 295K and the rest of the operating conditions to remain unchanged, the results of the calculations are shown in the figure 8.

| Run Path | | | Parameters for all Iterations (Done) | | | | | | |
|---|---|---|---|---|---|---|---|---|---|
| | | | mf1 | mf2 | outpressure | secinpressure | t3 | mfsecin | ratio |
| ✓ | 1 | 1 | 8.92E-4 | 0.001822 | 136000 | 97000 | 320 | 0.0045195608 | 0.4263108197 |
| ✓ | 1 | 2 | 8.92E-4 | 0.001822 | 136000 | 97000 | 330 | 0.0045638378 | 0.4304872796 |
| ✓ | 1 | 3 | 8.92E-4 | 0.001822 | 136000 | 97000 | 340 | 0.004433203 | 0.4181650582 |
| ✓ | 1 | 4 | 8.92E-4 | 0.001822 | 136000 | 97000 | 350 | 0.0043500452 | 0.410321139 |
| ✓ | 1 | 5 | 8.92E-4 | 0.001822 | 136000 | 97000 | 360 | 0.0043238779 | 0.4078528896 |
| ✓ | 1 | 6 | 8.92E-4 | 7.33E-4 | 97000 | 69000 | 320 | 0.0034450886 | 0.5427339579 |
| ✓ | 1 | 7 | 8.92E-4 | 7.33E-4 | 97000 | 69000 | 330 | 0.0033383884 | 0.5259245726 |
| ✓ | 1 | 8 | 8.92E-4 | 7.33E-4 | 97000 | 69000 | 340 | 0.0034256976 | 0.5396791296 |
| ✓ | 1 | 9 | 8.92E-4 | 7.33E-4 | 97000 | 69000 | 350 | 0.0033431221 | 0.5266703124 |
| ✓ | 1 | 10 | 8.92E-4 | 7.33E-4 | 97000 | 69000 | 360 | 0.0032308982 | 0.5089907318 |
| ✓ | 1 | 11 | 5.5E-4 | 0.0 | 51000 | 37000 | 320 | 0.0023124951 | 1.076361356 |
| ✓ | 1 | 12 | 5.5E-4 | 0.0 | 51000 | 37000 | 330 | 0.0022795864 | 1.061043852 |
| ✓ | 1 | 13 | 5.5E-4 | 0.0 | 51000 | 37000 | 340 | 0.0022459405 | 1.045383215 |
| ✓ | 1 | 14 | 5.5E-4 | 0.0 | 51000 | 37000 | 350 | 0.0022032417 | 1.025508864 |
| ✓ | 1 | 15 | 5.5E-4 | 0.0 | 51000 | 37000 | 360 | 0.0021910826 | 1.019849356 |
| ✓ | 1 | 16 | 2.74E-4 | 0.0 | 44000 | 34000 | 320 | 4.2395853E-4 | 0.3961072397 |
| ✓ | 1 | 17 | 2.74E-4 | 0.0 | 44000 | 34000 | 330 | 4.1870083E-4 | 0.3911949361 |
| ✓ | 1 | 18 | 2.74E-4 | 0.0 | 44000 | 34000 | 340 | 4.134904E-4 | 0.3863267971 |
| ✓ | 1 | 19 | 2.74E-4 | 0.0 | 44000 | 34000 | 350 | 4.1036968E-4 | 0.3834110879 |
| ✓ | 1 | 20 | 2.74E-4 | 0.0 | 44000 | 34000 | 360 | 4.0550559E-4 | 0.3788665366 |

Figure 8: Calculated results of secondary flow temperature changes are summarized in the table

Fig. 8 contains the corresponding nozzle flow rate, outlet pressure, secondary flow pressure, and secondary inflow port temperature $t_3$ for the four operating conditions of the electrostack, and the output parameters are the secondary flow rate of the ejector and the hydrogen reflux ratio. The nozzle flow rate is converted from the corresponding primary inflow pressure, and the use of mass flow rate instead of front-end pressure as an input is to avoid the replacement of boundary types during the automatic simulation.

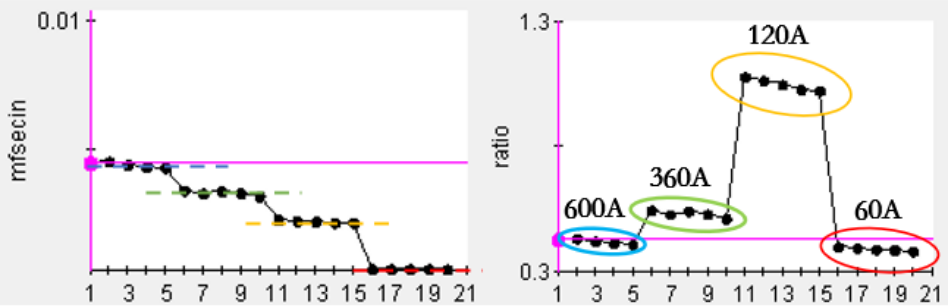


Figure 9: Trends of inject performance parameter ratios with secondary flow temperatures

As shown in Figure 9, compared to the primary flow temperature, the change in the secondary flow temperature has a smaller impact on the performance of the ejector, and the trend of the impact is opposite. Observing the impact effect graph of the secondary flow temperature on its mass flow rate, the latter does not change significantly with an increase in load current, and the point-line diagram is essentially consistent with the corresponding horizontal line. Observing specific values, it is evident that the secondary flow mass flow rate slightly decreases with an increase in its temperature, a change that is consistent with the trend of hydrogen recirculation ratio with temperature. This is because, in the simulation process of this section, the hydrogen molar component is fixed, and the hydrogen recirculation ratio is equal to the product of the secondary flow mass flow rate and the hydrogen mass fraction, hence both have the same rate of decline, a conclusion also derived from Figure 10.

The reason for the above phenomenon is that as the secondary flow temperature increases, the fluid density decreases, and the degree of this decrease cannot be compensated by the rising secondary flow velocity, leading to a decrease in their product, which results in a reduced mass flow rate through the recirculation pipe. Therefore, during the operation of PEMFC, maintaining a stable and appropriate temperature is crucial; too high a temperature can cause an increase in the anode return hydrogen temperature, leading to a decrease in the working performance of the ejector.

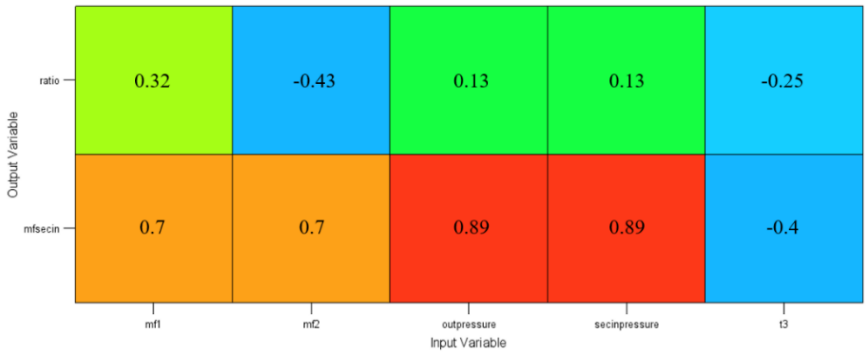


Figure 10: Plot of secondary flow temperature change variables

## 2.3 Influence of secondary inflow port temperature on elicitor performance

The secondary flow gas is not a pure gas; it includes water vapor and nitrogen. To study the impact of component changes on the ejector's performance, this section adopts molar fractions of water vapor components at 0.05, 0.1, 0.15, 0.2, and 0.25, with relative humidity increasing from 3.59% to 51%. This component increases with the rise in the fuel stack load, covering a wide range. The selection of the fuel stack conditions remains consistent with the previous section, with the primary flow temperature set at 295 K and the secondary flow temperature at 353 K, while other operating conditions remain unchanged. The calculation results are shown in the figure 11.

| Run Path | | | Parameters for all Iterations (Done) | | | | | | |
|---|---|---|---|---|---|---|---|---|---|
| | | | mf1 | mf2 | molarh2o | outpressure | secinpressure | mfsecin | secflowratio |
| ✓ | 1 | 1 | 8.92E-4 | 0.001822 | 0.05 | 136000 | 97000 | 0.0039424468 | 1.452633309 |
| ✓ | 1 | 2 | 8.92E-4 | 0.001822 | 0.1 | 136000 | 97000 | 0.0041375807 | 1.524532314 |
| ✓ | 1 | 3 | 8.92E-4 | 0.001822 | 0.15 | 136000 | 97000 | 0.0044453605 | 1.637936809 |
| ✓ | 1 | 4 | 8.92E-4 | 0.001822 | 0.2 | 136000 | 97000 | 0.0046668537 | 1.719548158 |
| ✓ | 1 | 5 | 8.92E-4 | 0.001822 | 0.25 | 136000 | 97000 | 0.0048290459 | 1.779309469 |
| ✓ | 1 | 6 | 8.92E-4 | 7.33E-4 | 0.05 | 97000 | 69000 | 0.0029675376 | 1.826176985 |
| ✓ | 1 | 7 | 8.92E-4 | 7.33E-4 | 0.1 | 97000 | 69000 | 0.0032605936 | 2.006519138 |
| ✓ | 1 | 8 | 8.92E-4 | 7.33E-4 | 0.15 | 97000 | 69000 | 0.0034323984 | 2.112245169 |
| ✓ | 1 | 9 | 8.92E-4 | 7.33E-4 | 0.2 | 97000 | 69000 | 0.0035550857 | 2.187745046 |
| ✓ | 1 | 10 | 8.92E-4 | 7.33E-4 | 0.25 | 97000 | 69000 | 0.0037541951 | 2.310273908 |
| ✓ | 1 | 11 | 5.5E-4 | 0.0 | 0.05 | 51000 | 37000 | 0.0020212072 | 3.674922182 |
| ✓ | 1 | 12 | 5.5E-4 | 0.0 | 0.1 | 51000 | 37000 | 0.0021546388 | 3.917525091 |
| ✓ | 1 | 13 | 5.5E-4 | 0.0 | 0.15 | 51000 | 37000 | 0.0022663423 | 4.120622364 |
| ✓ | 1 | 14 | 5.5E-4 | 0.0 | 0.2 | 51000 | 37000 | 0.0023919356 | 4.348973818 |
| ✓ | 1 | 15 | 5.5E-4 | 0.0 | 0.25 | 51000 | 37000 | 0.0024679734 | 4.487224364 |
| ✓ | 1 | 16 | 2.74E-4 | 0.0 | 0.05 | 44000 | 34000 | 3.7908703E-4 | 1.383529307 |
| ✓ | 1 | 17 | 2.74E-4 | 0.0 | 0.1 | 44000 | 34000 | 4.0041897E-4 | 1.461383102 |
| ✓ | 1 | 18 | 2.74E-4 | 0.0 | 0.15 | 44000 | 34000 | 4.1902915E-4 | 1.529303467 |
| ✓ | 1 | 19 | 2.74E-4 | 0.0 | 0.2 | 44000 | 34000 | 4.3593068E-4 | 1.590987883 |
| ✓ | 1 | 20 | 2.74E-4 | 0.0 | 0.25 | 44000 | 34000 | 4.5184739E-4 | 1.649078066 |

Figure 11: Calculated changes in secondary flow components are summarized in the table

To compare and analyze the impact of component changes on the ejector ratio, Figure 11 adds the ejector ratio to the output variables, on top of the secondary flow rate and hydrogen recirculation ratio. This value is the ratio of the ejector's secondary flow rate to the primary flow rate. Due to the changes in the water vapor molar component, the mass fraction of hydrogen changes accordingly. At this time, the hydrogen recirculation ratio is the product of the ejector ratio and the hydrogen mass fraction, with the conversion relationship between the hydrogen mass fraction and the water vapor molar fraction as shown in Formula 4.

$$secflowratio = \omega = \frac{mf_{secin}}{mf_{firin}} \tag{2}$$

$$ratio = \omega_{H_2} = secflowratio \cdot W_{H_2} \tag{3}$$

$$W_{H_2} = \frac{M_{H_2} \cdot m_{H_2}}{M_{H_2} \cdot m_{H_2} + M_{N_2} \cdot m_{N_2} + M_{vapor} \cdot m_{vapor}} \tag{4}$$

Where $W_{H_2}$ represents hydrogen mass fraction; $m_{H_2}$ represents mole fraction of hydrogen; $M_{H_2}$ represents molar mass of hydrogen.

The results of the calculations are shown in Figures 12 and 13, where the dotted line plots of the variation of the hydrogen reflux ratio A with the water vapor fraction are plotted by calculating the corresponding hydrogen mass fraction.

The calculation results are shown in Figures 12 and 13, where the point-line graph of the hydrogen recirculation ratio A changing with the water vapor component is drawn after calculating the corresponding hydrogen mass fraction. Observing Figure 12, it is found that as the water vapor component in the secondary flow increases, both the secondary flow rate and the ejector ratio increase. Specifically, at a load current of 600A, the growth rate of the secondary flow rate is 22.6%, at 360A it is 26.5%, and at 120A and 60A, the growth rates are 22.1% and 19.2%, respectively. As the current increases, the growth rate of the ejector ratio is 19.1%, 22.1%, 26.5%, and 22.49%, with the maximum growth rate occurring at 120 A, and the rest of the load conditions changing similarly. From Figure 13, it is observed that as the water vapor component in the secondary flow increases, the hydrogen recirculation ratio of the ejector decreases, with the most significant drop at 120A, while the decrease rates under other responsible conditions are similar. This is opposite to the changes in the secondary flow mass and the ejector ratio shown in Figure 12.

The above phenomenon is caused by the increase in the water vapor component in the secondary flow gas. According to the formula for calculating the mass fraction of the mixture, the mass of the mixed gas is determined by the proportion of each component and its corresponding molar mass. The molar mass of water vapor is 18 g/mol, while that of hydrogen is 2 g/mol. With the increase in the water vapor component, the proportion of substances with greater mass increases, leading to an overall mass increase in the mixed gas, producing the phenomenon shown in Figure 12.

However, the ejector ratio and hydrogen recirculation ratio do not both represent the performance of the ejector. The amount of hydrogen mass in the secondary flow is the key to determining the performance of the hydrogen fuel cell ejector. When the nitrogen component in the mixed gas remains constant, the rise in the water vapor component causes a decrease in the hydrogen component, producing the phenomenon shown in Figure 13. This phenomenon often occurs in the case of improper thermal management of the fuel stack, where the temperature of the secondary flow recirculated hydrogen increases, the saturated vapor pressure of the mixed gas rises, the gas can accommodate more water vapor, causing the ejector hydrogen recirculation ratio to decrease, leading to a decline in overall performance.

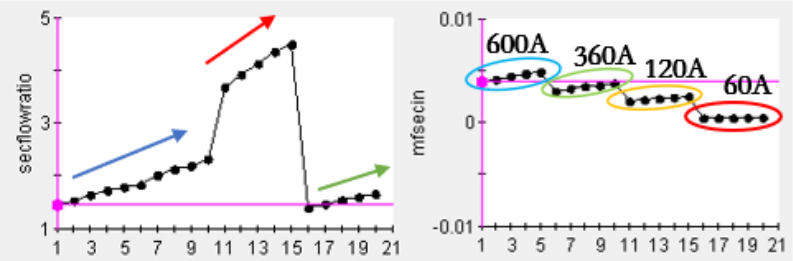


Figure 12: Trends of ejector ejection ratio and secondary flow rate with secondary flow components

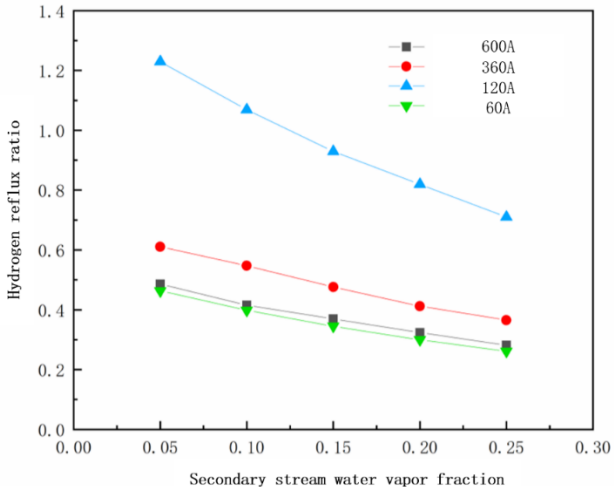


Figure 13: Trend of hydrogen reflux ratio of ejector with secondary flow components

## 3. Comparison of results

Based on the above research, the impact of operating conditions of coaxial nozzle ejectors on their performance and optimization methods were clarified. This paper compares the optimized coaxial nozzle ejector with traditional single-nozzle ejectors with different nozzle cross-sectional areas in terms of hydrogen recirculation ratio across the entire power range of the fuel stack, with comparative results shown in Figure 14. In Figure 14, 1.15mm and 0.65mm represent the nozzle cross-sectional radii of traditional single-nozzle ejectors, with their calculated areas corresponding to the total cross-sectional area of the dual nozzles of the coaxial nozzle ejector and the area of the smaller nozzle, respectively. At low load segments, the hydrogen recirculation ratio of the 0.65mm single-nozzle ejector and the coaxial nozzle ejector in dual-nozzle mode are essentially identical, where only the smaller nozzle of the coaxial nozzle ejector operates, making it indistinguishable from the traditional single-nozzle ejector. However, the former is limited by the maximum pressure in front of the proportional valve and can only operate normally between 0.27 g/s and 0.96 g/s. Compared to the

former two, the large nozzle mode coaxial nozzle ejector and the 1.15mm single-nozzle ejector do not perform ideally at low load segments, with a narrower effective working area, lacking advantages.

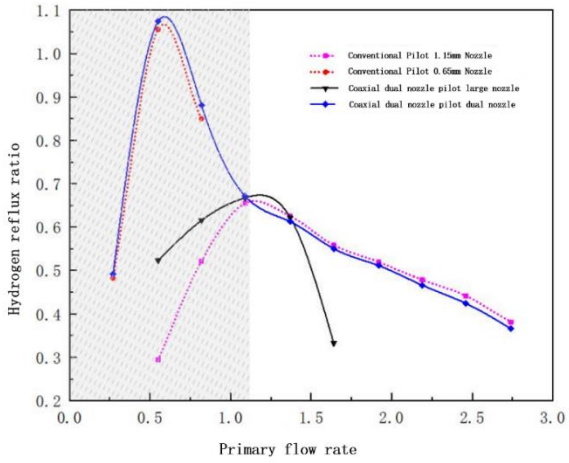


Figure 14: Full Operating Condition Comparison between Coaxial Nozzle Ejector and Traditional Single-Nozzle Ejector

The primary flow rate increases further, within the range of 1.09g/s to 1.37g/s, the large nozzle mode coaxial nozzle ejector performs better, while the 1.15mm single-nozzle ejector performs slightly better than the coaxial nozzle ejector in dual-nozzle mode. After the primary flow rate exceeds 1.37g/s, the 1.15mm single-nozzle ejector performs slightly better than the coaxial nozzle ejector in dual-nozzle mode, but both show consistent trends. This is because, under such conditions, the coaxial nozzle ejector operates with both the annular nozzle and the small nozzle open. There exists an angle A between the jets of the former and the latter, and the collision between the two jets leads to energy loss. This makes the performance of the coaxial nozzle ejector slightly inferior to that of the traditional single-nozzle ejector in the medium and high power sections, as shown in the following figure:

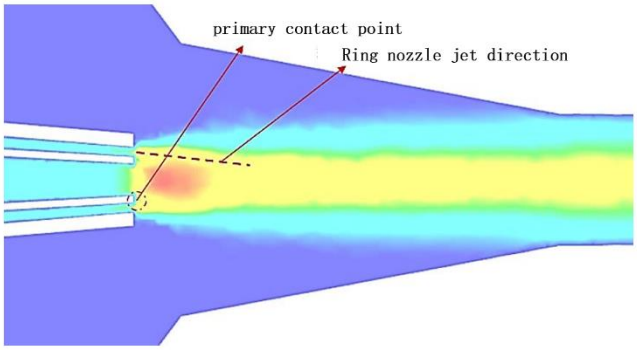


Figure 15: Nozzle Jet Contact Schematic

In summary, within the shaded area in Figure 15, the coaxial nozzle ejector demonstrates better performance compared to the traditional single-nozzle ejector. By switching the working mode of the nozzle, it effectively addresses the issue of the narrow effective working range caused by the fixed nozzle cross-section limitation of traditional single-nozzle ejectors, as well as the inability to accommodate both high and low load segments of the fuel stack, thereby expanding the coverage range of the ejector.

## 4. Conclusion

This paper establishes an automatic simulation platform based on ISIGHT to explore the impact of

primary flow temperature, secondary flow temperature, and components on the working performance of coaxial nozzle ejectors. It is found that the performance of the ejector improves with an increase in primary flow temperature, while the opposite effect is observed when the secondary flow temperature and water component content increase, leading to suggestions for improving the performance of the ejector. A comparison of the working performance of coaxial nozzle ejectors and traditional single-nozzle ejectors under different load conditions of the fuel stack reveals that coaxial nozzle ejectors have a broader working range and better performance in the low load segment of the fuel stack.

## References


*[1] Liu ZY, Chen J, Liu H, Yan CZ, Hou Y, He QG, et al. Anode purge management for hydrogen utilization and stack durability improvement of PEM fuel cell systems. Appl Energy 2020; 275:115110.*

*[2] Wang XH, Xu SC, Xing CM. Numerical and experimental investigation on an ejector designed for an 80 kW polymer electrolyte membrane fuel cell stack. J Power Sources 2019; 415:25e32.*

*[3] Hong ZH, Li Q, Han Y, Shang WL, Zhu YN, Chen WR. An energy management strategy based on dynamic power factor for fuel cell/battery hybrid locomotive. Int J Hydrogen Energy 2018;43:3261e72.*

*[4] Wang BW, Wu KC, Xi FQ, Xuan J, Xie X, Wang XY, et al Numerical analysis of operating conditions effects on PEMFC with anode recirculation. Energy 2019;173:844e56.*

*[5] Hwang JJ. Passive hydrogen recovery schemes using a vacuum ejector in a proton exchange membrane fuel cell system. J Power Sources 2014;247:256e63.*

*[6] R. Parsons, H.K. Ersoy. Performance characteristics of the ejector refrigeration system. Conversion & Management [M]. 1901*

*[7] L Munday JT, Bagster D F. A new theory applied to steam jet refrigeration. Int. En l Chem Proc DD, 1977, 16: 442-449.*

*[8] Javier Valle, J. Jabardo. A one dimensional model for the determination of an ejector entrainment ratio[J]. International Journal of Refrigeration, 2012, 35:772-784*

*[9] Randheer L. Yadav, Ashwin W. Design aspects of ejectors: Effects of suction chamber geometry[J]. Chemical Engineering Science, 2008, 63: 3886 -3897.*

*[10] S. Aphornratana, Eames. I. W. A small capacity steam ejector refrigerator: experimental investigation of a system using ejector with movable primary nozzle [J]. International Journal of Refrigeration, 1997, 20:352-358.*

*[11] Brunner D A, Marcks S, Bajpai M, et al. Design and characterization of an electronically controlled variable flow rate ejector for fuel cell applications [J. Int J Hydrogen Energ, 2012, 37: 4457-4466.*

*[12] Lwy K M, Cs K. Development of the variable multi-ejector for a mini-bus PEMFC system. In : ECS fuel cell seminar 30-honolulu, Hawai (November 13-November 17, 2006)[J]. ECS transactions, 2007. 773-780.*

*[13] Han J Q, Feng M, Hou 'T F, et al. Performance investigation of a multi-nozzle ejector for proton exchange membrane fuel cell system [J]. Int J Energ Res, 2021, 45: 3031-3048.*